



Tribological performance of titanium samples oxidized by fs-laser radiation, thermal heating, or electrochemical anodization

S. V. Kirner¹ · N. Slachciak¹ · A. M. Elert¹ · M. Griepentrog¹ · D. Fischer¹ · A. Hertwig¹ · M. Sahre¹ · I. Dörfel¹ · H. Sturm¹ · S. Pentzien¹ · R. Koter¹ · D. Spaltmann¹ · J. Krüger¹ · J. Bonse¹ 

Received: 27 October 2017 / Accepted: 15 March 2018
© The Author(s) 2018

Abstract

Commercial grade-1 titanium samples (Ti, 99.6%) were treated using three alternative methods, (i) femtosecond laser processing, (ii) thermal heat treatment, and (iii) electrochemical anodization, respectively, resulting in the formation of differently conditioned superficial titanium oxide layers. The laser processing (i) was carried out by a Ti:sapphire laser (pulse duration 30 fs, central wavelength 790 nm, pulse repetition rate 1 kHz) in a regime of generating laser-induced periodic surface structures (LIPSS). The experimental conditions (laser fluence, spatial spot overlap) were optimized in a sample-scanning setup for the processing of several square-millimeters large surface areas covered homogeneously by these nanostructures. The differently oxidized titanium surfaces were characterized by optical microscopy, micro Raman spectroscopy, variable angle spectroscopic ellipsometry, and instrumented indentation testing. The tribological performance was characterized in the regime of mixed friction by reciprocating sliding tests against a sphere of hardened steel in fully formulated engine oil as lubricant. The specific tribological performance of the differently treated surfaces is discussed with respect to possible physical and chemical mechanisms.

1 Introduction

Titanium is a technologically relevant metal with high corrosion and temperature resistance, good biocompatibility, and an extraordinary strength-to-weight ratio. These properties render it attractive for industrial, aeronautical, or medical applications [1]. In previous publications [2–4] we already reported the beneficial effect of the femtosecond (fs) laser processing of titanium surfaces (compared to the polished reference surface) for tribological applications. A significant reduction of friction and wear was reported if a 100Cr6 ball of steel in engine oil as lubricant (regime of mixed friction) is used for reciprocating sliding experiments on fs-laser processed titanium (Ti) or titanium alloy (Ti6Al4V). The fs-laser processing was performed at conditions where sub-micrometer sized nanostructures (so-called low spatial frequency LIPSS, LSFL [5–7]) were formed, covering the treated surface homogeneously. The positive tribological effect was attributed to the presence of additives contained in

the engine oil covering the laser structured surfaces and preventing a direct metal to metal contact [2, 3]. It was proven that the LSFL nanostructures in the wear track endured the tribological tests. As the beneficial tribological effect was not observed at the (non-irradiated) polished reference surface, it was speculated already in [3] that the tribological performance might be further promoted by laser-induced chemical reactions such as oxidation at the titanium surface.

In this work, we perform additional experiments to elucidate the relevance of superficial oxidation on the tribological performance of titanium surfaces by comparing two traditional ways of surface engineering via thermal and anodic oxidation with the fs-laser processing method. The impact of the oxide layer thickness, its material structure and the superficial hardness are related to the current knowledge of tribological mechanisms acting for lubricants with additives.

2 Experimental

The flat surfaces of cylinders of 24 mm diameter and 8 mm thickness of grade-1 titanium (Ti, 99.6%, Schumacher Titan GmbH, Solingen, Germany) samples were mechanically

✉ J. Bonse
joern.bonse@bam.de

¹ Bundesanstalt für Materialforschung und -prüfung (BAM),
Unter den Eichen 87, 12205 Berlin, Germany

polished, resulting in a mirror-like surface finish with an average roughness $R_a < 10$ nm.

A commercial Ti:sapphire femtosecond laser amplifier system (Femtolasers, Compact Pro) was used to generate linearly polarized laser pulses ($\tau = 30$ fs pulse duration, $\lambda = 790$ nm center wavelength, $f = 1$ kHz pulse repetition frequency). The laser pulses were focused by a spherical dielectric mirror of 500 mm focal length onto the sample surface. The titanium samples were mounted on a motorized x - y - z linear translation stage and placed normal to the incident laser beam, a few millimeters in front of the geometrical laser focus where a Gaussian-like spatial beam profile with a $1/e^2$ -decay radius $w_0 \sim 140$ μm was measured. All irradiation experiments were performed in air. If not stated differently, the peak laser fluence was adjusted to $\Phi_0 \sim 0.11$ J/cm^2 , enabling the generation of LSFL [2, 3, 5, 6]. A square area of 5×5 mm^2 was processed by meandering movement of the sample (scan velocity $v_x = 1$ mm/s, line-offset $\Delta y = 0.1$ mm). At these conditions, the effective number of laser pulses (N_{eff}) per focused laser spot diameter $D = 2w_0$ accounts to $N_{\text{eff}} = D \times f/v_x \sim 56$ in the scan direction (for a single laser processing pass). Using an ultrasonic bath, the samples were cleaned in acetone after the laser processing. In previous publications, we have shown that these structures on titanium are oriented perpendicular to the fs-laser beam polarization with lateral (spatial) periods of (520 ± 80) nm, and vertical modulation depths of a few hundreds of nanometers [3, 4, 6].

Two samples were placed in an oven and exposed to a temperature (T) for a duration (t) in ambient atmosphere. The first sample (THERMOX-1) was placed for $t_1 = 5$ min. in the oven pre-heated to a temperature of $T_1 = 750$ $^\circ\text{C}$, while the second sample (THERMOX-2) was treated at $T_2 = 450$ $^\circ\text{C}$ for $t_2 = 180$ min. For electrochemical treatment, the samples were anodized in a two-electrode cell at room temperature, using a Pt sheet as a counter-electrode. First, the electrically wired Ti sample was vertically oriented and dipped ~ 20 mm deep into 1 M H_2SO_4 , while anodization was performed for two minutes at 9 V. Then, the sample was lifted by ~ 10 mm and another anodization step was performed for two more minutes at 18 V. The anodization led to a characteristic change of the color of the sample surface caused by thin film interference effects due to differently thick oxide layers. The surface region anodized at 9 V turned to a yellowish-brown color (referred to as ANOX-9V in the following). The other surface region, which was additionally anodized at 18 V, turned dark blue and is named ANOX-18V. After the anodization steps, the sample was rinsed with deionized water and blow-dried with nitrogen. All differently oxidized samples were characterized by optical microscopy (OM), scanning electron microscopy (SEM), micro Raman spectroscopy (μ -RS), variable angle spectroscopic ellipsometry (VASE), and instrumented indentation testing (IIT).

Micro Raman spectroscopy (μ -RS) was used for probing structural changes in the laser-modified regions. All Raman spectra were recorded in backscattering geometry by a WiTEC 300R Alpha device. The spectra are presented without background correction. A ruled 1800 grooves/mm grating was chosen in the optical spectrometer (WiTEC, UHTS 300), which was equipped with a Peltier-cooled CCD camera (ANDOR, iDus DV401A) operated at a temperature of 210 K. The resulting wavenumber resolution is < 2 cm^{-1} . The fs-laser irradiated surface regions were excited at a power level of 4 mW using the 488 nm emission line of a continuous wave laser (Spectra Physics, Excelsior). The Raman-laser radiation was focused on the sample surface by a microscope objective (Zeiss, EC Epiplan 20 \times , NA 0.4) probing a circular spot of ~ 4 μm in diameter.

The thickness of the titanium oxide layers was determined using *Variable Angle Spectroscopic Ellipsometry* (VASE). The ellipsometric quantities Ψ and Δ were measured with a Woolam M-2000DI Ellipsometer in the spectral range of 190 to 1700 nm at angles from 55° to 75° in 5° steps. At 75° an elliptical surface area of 3×12 mm^2 is probed. The data were fitted with the WVase32 software (version 3.81) using a generalized oscillator model [8] for the titanium oxide layer as well as the metallic titanium substrate. To establish a proper reference for the dielectric function of the substrate, a polished titanium surface was measured without further treatment.

Instrumented Indentation Testing (IIT) is a suitable method to determine the mechanical properties of thin laser-irradiated surface layers, since depth-dependent quantities are obtained [9]. The Keysight G200 Nanoindenter system, equipped with an XP measuring head system, was used for this investigation. The nanoindentation testing procedure was performed using the international standard ISO 14577 [10] for metallic materials. Depth-dependent indentation measurements were performed with a calibrated Berkovich diamond indenter (AccuTip by Keysight Technologies) with a nominal tip radius of less than 50 nm. On every sample, 25 indentations (raster 5×5 , distance 20 μm) were located close to the center of the region of interest.

The indentation was performed by displacement control, either to a depth of 500 nm to reveal details close to the surface or at larger depths up to 2000 nm to get information on the pristine material. From the load–displacement data, mechanical properties such as hardness and elastic modulus can be determined without ex-situ imaging of the indentation sites. The samples were measured using the Continuous Stiffness Method (CSM) [11–13]. For these measurements, the indenter oscillates with an amplitude of 2 nm and a frequency of 45 Hz during the loading segment. All values of the indentation hardness H_{IT} have been calculated from the measured contact stiffness at a given indentation depth, without considering any substrate influence.

Reciprocating sliding tribological tests (RSTT) were performed in a home-made tribometer by sliding the samples at a normal force of $F_N = 1.0$ N against a hardened and polished ball (diameter 10 mm; average roughness $R_a \sim 6$ nm) made of 100Cr6 steel as counter body. The velocity between sample and ball follows a sine function with its maximum value in the middle of the stroke distance of 1 mm total length. During the movement, the frictional forces acting on the sample are recorded. From this information and the known normal force, the coefficient of friction (COF) can be quantified [14]. The radius of the ball-sample contact was estimated using a Hertzian deformation model (HDM) of a sphere in contact with a flat sample. For the specific normal force applied, the ball diameter used here and the material combination tested (hardness of titanium and hardened 100Cr6 steel), a contact radius of ~ 36 μm and a deformation of ~ 260 nm are estimated by the HDM, associated with average and maximum contact pressures of ~ 240 MPa and ~ 370 MPa, respectively [15]. In the RSTT experiments, 1000 cycles were performed at a frequency of 1 Hz in fully formulated engine oil (Castrol VP-1). The range of uncertainty in the friction coefficient measurements is ± 0.02 . After the tribological tests, the samples were cleaned in petroleum ether for 5 min. using an ultrasonic bath to remove the residual lubricant and wear particles. Subsequently, the corresponding wear tracks were inspected by OM and SEM. Selected wear tracks were characterized by *Scanning Transmission Electron Microscopy* (STEM) of cross-sections normal to the sample surface. For that, the sample was prepared by a focused ion beam (FIB) milling machine Quanta 3D from FEI using the in-situ lift-out technique [16]. The preparation of the TEM lamella starts by deposition of a protective Pt cap layer at the region of interest. Via several process steps, a trench of the material is formed and thinned by Ga-ions up to electron-transparency. This lamella of ~ 100 nm thickness was investigated in a scanning transmission electron microscope JEM 2200FS (JEOL) operated at 200 kV. It is equipped with a field emission gun, an in-column energy filter and an energy dispersive X-ray (EDX) spectroscopy system. The point resolution of the STEM is better than 0.25 nm.

3 Results and discussion

Many of the beneficial properties of titanium arise from the oxidation behavior of its surface. Hence, it is instructive to discuss briefly the thermal oxidation of titanium found in the literature to provide a basis for the discussion of the results presented in the following Sects. 3.1–3.4. Due to its high affinity to oxygen, titanium may undergo several modifications. In air, the thermodynamically most stable oxide is TiO_2 , which exists in three different modifications, namely anatase, brookite, and rutile [17]. Upon heating

of mechanically polished cast titanium in air at a rate of 5 $^\circ\text{C}/\text{min}$. to temperatures exceeding ~ 275 $^\circ\text{C}$, the surface passivating oxide layer (TiO_2) converts into a crystalline film consisting mainly of anatase [18]. At approx. 445 $^\circ\text{C}$, rutile starts to nucleate and the oxide film then consists of anatase and rutile sub-layers. For temperatures exceeding 600 – 650 $^\circ\text{C}$, the growth rate of the oxide layer follows a parabolic law, accompanied by a significant increase of the layer thickness [17, 18]. Above ~ 720 $^\circ\text{C}$, the anatase converts into the thermodynamically most stable polymorph rutile [18].

To compare the surface morphologies of the differently oxidized samples presented in this work, Fig. 1 provides overview SEM micrographs (left column) along with detailed magnifications (right column) of typical surface regions on all samples. The smoothest surface is observed for the POLISHED sample, while pronounced LIPSS with periods between 500 and 600 nm are present at the surface of the LASOX sample. Both THERMOX samples reveal grainy surfaces, along with indications of a heterogeneous delamination of a thin superficial layer (more pronounced at the THERMOX-1 surface). The two ANOX samples appear similar in the overview images, while some local differences can be discerned at higher magnifications.

3.1 Structural analysis: micro Raman spectroscopy

Figure 2 compiles Raman spectra acquired in the wavenumber range between 50 and 700 cm^{-1} from six different sample areas, i.e., the flat reference surface (POLISHED) and the fs-laser irradiated area (LASOX) (Fig. 2a), the thermally treated samples (THERMOX-1 and THERMOX-2) (Fig. 2b), and the anodically oxidized surfaces (ANOX-9V and ANOX-18V) (Fig. 2c). Note that an offset of about 160 counts per second (cps) is present due to detector's noise in all $\mu\text{-RS}$ spectra.

The Raman signal of the polished titanium surface (dark cyan curve) exhibits a very broad low-level background along with some almost vanishing peaks at 93, 108, 141, and 337 cm^{-1} . The peak located at 141 cm^{-1} matches the value of (135 ± 2) cm^{-1} reported by Nemanich et al. for the E_{2g} mode of the hexagonal close-packed phase of a 6 nm thick titanium film [19]. The origin of the other specific peaks at 93, 108, and 337 cm^{-1} is currently not clear. However, their distinct sharp form is an evidence for a crystalline origin.

The brown curve in Fig. 2a represents the Raman spectrum acquired on the fs-laser oxidized surface regions, which are covered by LSFL. The spectrum consists of a broad peak maximizing at ~ 210 cm^{-1} along with a wide shoulder around 460 cm^{-1} , which is consistent with the formation of amorphous material. Very similar spectra were reported by Landis et al. [20] and Shinonaga et al. [21] for fs-laser generated LSFL on titanium surfaces. The spectrum can be attributed to the formation of amorphous TiO_2 [20–22].

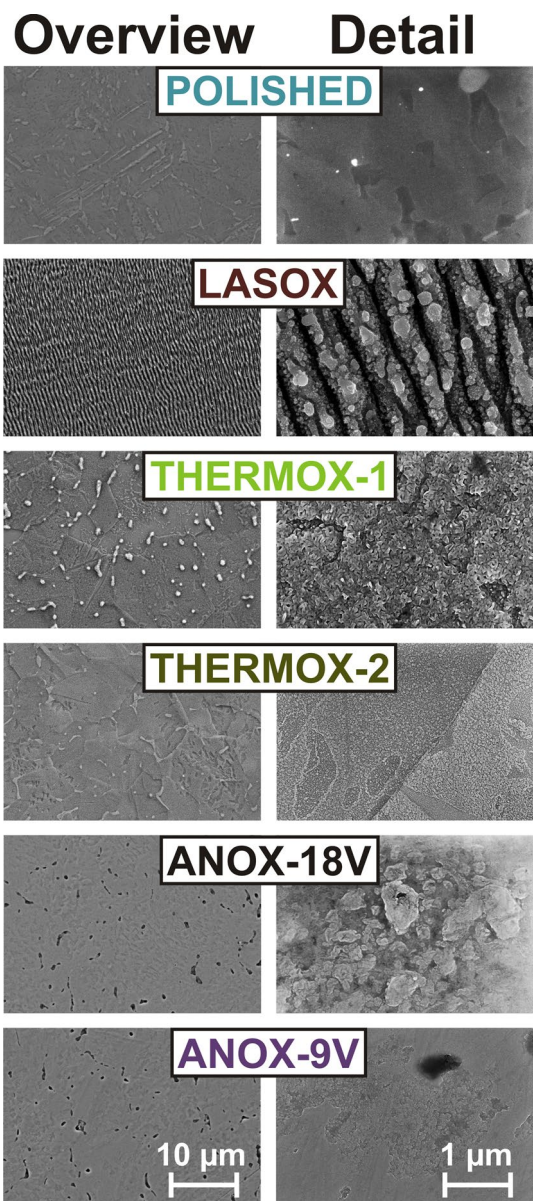


Fig. 1 Scanning electron micrographs of the differently oxidized grade-1 titanium samples. Left column: overview images taken in secondary electron mode. Right column: Detailed magnifications acquired in the InLens mode. At the bottom images, a common scale bar is provided for each column

Given the large width of the peaks, contributions of other amorphous titanium oxides are possible.

Figure 2b displays the μ -RS spectra of the two thermally treated samples. Both spectra show a broad background consistent with the formation of amorphous titanium oxides along with three characteristic peaks at 245, 444, and 611 cm^{-1} . These peaks are indicative of the rutile phase of TiO_2 and are labelled “R” in the graph [23]. The signal acquired from the sample THERMOX-1 is 2.5–4.5 times

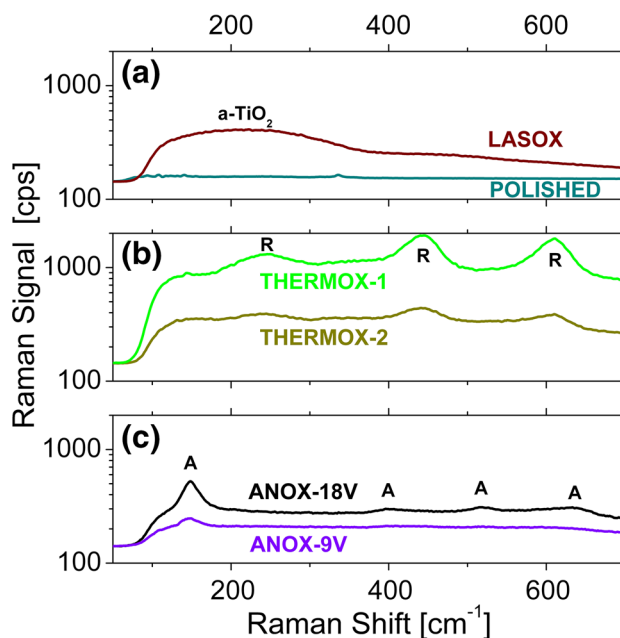


Fig. 2 Raman spectra of differently oxidized grade-1 titanium samples. **a** LSFL-covered surface regions after processing by fs-laser pulses in air (LASOX: brown curve). A reference spectrum of the non-irradiated sample surface is shown for comparison (POLISHED: dark cyan curve); **b** Thermally treated samples (THERMOX-1: green curve, THERMOX-2: dark yellow curve); **c** Anodically oxidized samples (ANOX-18V: black curve, ANOX-9V: purple curve). An offset of about 160 cps is present due to detector’s noise. “A” and “R” indicate the Raman peak positions of anatase and rutile, respectively. Note the logarithmic scale of the ordinates. The data in **a** are taken from Ref. [27]

larger than that of THERMOX-2, which points to a significantly thicker oxide layer in case of THERMOX-1.

Figure 2c shows the μ -RS spectra of the two anodically oxidized samples. As seen for the laser- and thermally oxidized titanium samples, both spectra exhibit a broad background signal. Four characteristic peaks can be discerned at 148, 400, 517, and 634 cm^{-1} , which are all attributed to the anatase phase of TiO_2 (labelled “A” in the graph) [24]. The signal recorded at the sample ANOX-18V is 1.3 to 3.5 times larger than that of ANOX-9V indicating again an increased oxide layer thickness. Moreover, the anatase peaks are more pronounced for ANOX-18V.

No peaks of rutile are present in the spectra of the anodically oxidized samples (Fig. 2c). Vice versa, no peaks of anatase are seen in the thermally treated samples (Fig. 2b). It is concluded that thermal treatment at temperatures above 450 $^{\circ}\text{C}$ favors the formation of the rutile phase, while the anodic oxidation performed at room temperature leads to the formation of anatase.

Complementary X-ray diffraction (XRD) analyses were performed under grazing incidence conditions for probing surface near layers. These XRD measurements were carried

out in the angular range 2θ between 23° and 33° , where all polymorphs of TiO_2 exhibit distinct peak positions. The XRD results (data not shown here for brevity) fully confirmed our Raman spectroscopic analyzes, i.e., (i) the two regions on the ANOX sample only show the presence of anatase without indications of rutile, (ii) the two THERMOX samples revealed the presence of rutile only, and (iii) the LASOX sample did not show any peaks due to the amorphous nature of the probed material.

3.2 Thickness determination: variable angle spectroscopic ellipsometry

The Raman spectra indicate that the oxide layer thickness may vary among the differently oxidized samples. To determine the thickness of the oxide layers, VASE was performed. The thickness of the titanium oxide layers was extracted from the VASE experiments by modelling the respective dielectric function of the layer material as well as the substrate. This was done by utilizing a generalized oscillator model, which combines several mathematical expressions to simulate the dielectric function.

The substrate material (metallic titanium) was modelled by three harmonic oscillators for the visible part and a Drude function for the infrared part of the spectrum. The resulting model led to sufficient least-squares-fits of the ellipsometric data, as seen in Fig. 3a. For brevity, the ellipsometric quantities Ψ and Δ are shown here only for an angle of incidence of 60° . This analysis revealed that a ~ 3.8 nm native oxide layer is present on top of the polished titanium substrate. This native oxide was modelled using a Tauc–Lorentz function [25].

In the next step, the substrate dielectric function was kept constant and the four different titanium oxide layers were analyzed for the thermally and anodically treated samples. For three of those four samples (THERMOX-2, ANOX-18V, and ANOX-9V), the same model was used which consists of a Cody–Lorentz function [26] to fit the bandgap region of TiO_2 at energies of 3.2–3.4 eV, a Gaussian function to model absorption in the ultraviolet and a Drude function for free-carrier absorption in the infrared part of the spectrum. In case of THERMOX-1, a more complex model was developed. Here, it was found that a two-layer approach is necessary for a sufficient fit of the ellipsometric data: the first layer was modelled as a combination of a Tauc–Lorentz (bandgap), a Gaussian function (visible absorption peak) and a Lorentz oscillator (free-carrier absorption). The second layer was modelled as a Tauc–Lorentz function for considering the optical bandgap along with three additional harmonic oscillators to simulate absorption peaks over the complete spectral range measured. An additional roughness layer was added to the models of each sample including a 50% effective medium approximation of the underlying layer material.

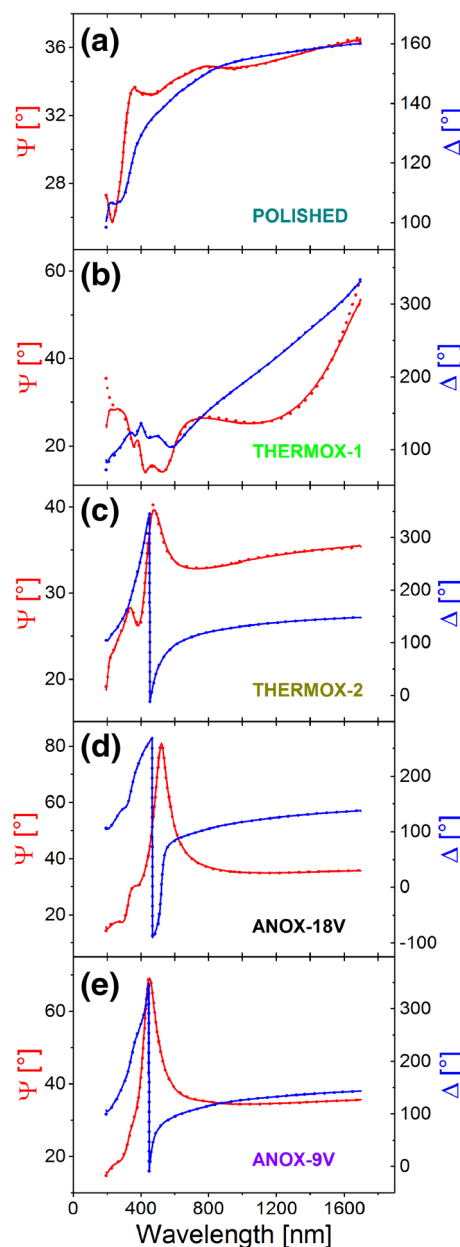


Fig. 3 Ellipsometric quantities Ψ and Δ vs. wavelength of differently oxidized grade-1 titanium samples as measured by VASE at an angle of incidence of 60° . **a** Reference spectra of the non-irradiated sample surface (POLISHED); **b–c** Spectra of the thermally treated samples (THERMOX-1 and THERMOX-2); **d–e** Spectra of the anodically oxidized samples (ANOX-18V, ANOX-9V). The solid lines represent the measured data, the dashed lines the least-squares-fits to the corresponding models. Note the different scales of the ordinates

The resulting fits for all samples are shown in Fig. 3b–e. The respective values for the titanium oxide layer thickness and the corresponding roughness are presented in Table 1.

The interpretation of these resulting oxide layer thicknesses allows a correlation with the data obtained by Raman spectroscopy. It was shown, that ANOX-18V generally

Table 1 List of differently oxidized grade-1 titanium samples along with relevant oxide layer properties determined by VASE (thickness), μ -RS (Type of oxide) and IIT (hardness)

Sample name	Oxide layer thickness + roughness layer thickness (nm)	Type of oxide	Indentation hardness (GPa)
POLISHED	~3.8	a-TiO ₂ [22]	2.2 ± 0.2
LASOX	> 200 [27]	a-TiO ₂ /nc-TiO ₂	1.3 ± 0.2
THERMOX-1	150 + 12	a-TiO ₂ /rutile	8.4 ± 2.2
THERMOX-2	22 + 6	a-TiO ₂ /rutile	3.2 ± 0.3
ANOX-18V	47 + 9	a-TiO ₂ /anatase	3.2 ± 0.4
ANOX-9V	41	a-TiO ₂ /anatase	3.0 ± 0.3

exhibits a higher signal count than ANOX-9V. This implies that the thickness of the probed material is larger for ANOX-18V, as verified by ellipsometry (56 nm oxide layer thickness for ANOX-18V compared to 41 nm for ANOX-9V). The same correlation is seen for THERMOX-1 (162 nm) and THERMOX-2 (28 nm). However, due to the significant differences in modelling of THERMOX-1, it can be assumed that the surface layer consists of more than one phase of TiO₂. This is again in line with the Raman spectra shown in Fig. 2b, where more pronounced contributions of rutile were detected in THERMOX-1 along with the signature of amorphous TiO₂ that is present in both thermally oxidized samples.

The determination of the thickness of the laser-induced oxide layer at the surface of the LASOX sample by VASE was more complicated, since the ellipsometric signals showed a significant dependence on the orientation of light polarization with respect to that of the LSFL nanostructures. Consequently, it was not possible to fit the data to a simple model of titanium covered by oxide layers with pronounced (sharp) interfaces (data not shown here). While polarization anisotropy is caused by optical scattering and diffraction at the sub-wavelength sized grating-like LSFL surface topography, the ellipsometric data suggest that depth graded oxide layers without sharp interfaces were formed upon fs-laser irradiation. The latter hypothesis was confirmed by depth-profiling Auger electron spectroscopy, which revealed that the thickness of the oxide layer in LSFL-covered regions on titanium exceeds 200 nm [27]. This finding is fully in line with earlier estimates of the heat-affected zone (HAZ) observed in fs-laser irradiation of another titanium-containing compound material (TiN), which extends up to ~300 nm into the depth of the processed material [28].

3.3 Hardness measurements

Another factor that may influence the tribological performance of the samples is the hardness of the material. Here, the fact that a thin superficial oxide layer may exhibit a different hardness than the bulk of the titanium material underneath is taken into consideration. To record the major

influence of the substrate material in traditional hardness measurements, the method of IIT was chosen to characterize the indentation hardness at depths which are typical for the initial plastic deformation in the tribological tests performed within this work (see Sect. 3.4), i.e., at sub-micrometer surface displacements. Figure 4 summarizes the measurements of the indentation hardness H_{IT} (in GPa) versus the displacement (depth) of the indenter for all six samples investigated. For comparison, the bulk value of $H_{IT,bulk} \sim 1.95$ GPa (as

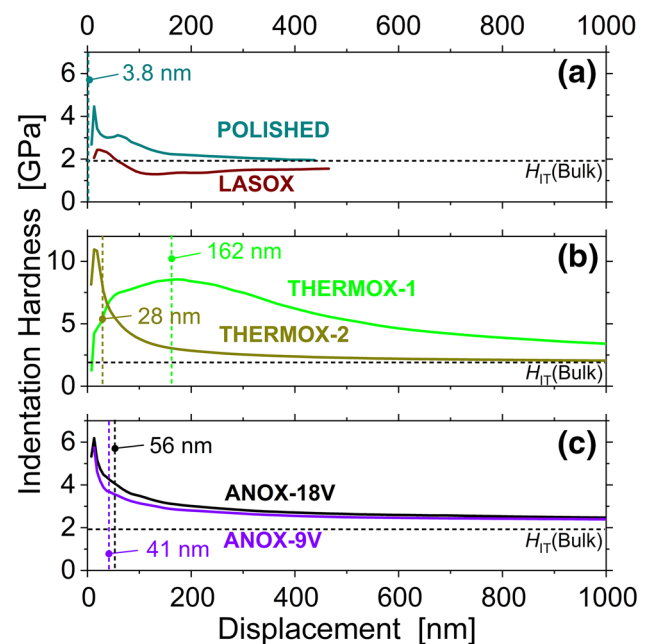


Fig. 4 Indentation hardness vs. displacement of the indenter of differently oxidized grade-1 titanium samples. **a** LSFL-covered surface regions after processing by fs-laser pulses in air (LASOX: brown curve). A reference spectrum of the non-irradiated sample surface is shown for comparison (POLISHED: dark cyan curve); **b** thermally treated samples (THERMOX-1: green curve, THERMOX-2: dark yellow curve); **c** Anodically oxidized samples (ANOX-18V: black curve, ANOX-9V: purple curve). The horizontal lines indicate the indentation hardness of the bulk material [$H_{IT}(\text{Bulk})$]. The vertical dashed lines indicate the total thickness of the oxide layers as obtained by VASE (oxide layer thickness + roughness layer thickness, see Table 1). Note the different scales of the ordinates

measured at displacements of ~ 2000 nm) is shown for the titanium samples as horizontal dashed line. This value is in good agreement with the results given in reference [29]. The colorized vertical dashed lines indicate the corresponding values of the oxide layer thickness as obtained from the modelling of the VASE measurements provided in the previous Sect. 3.2.

The thicknesses of the oxide films determined from the ellipsometric measurements agree within a deviation of less than 30 nm with the displacement at which the peak values of H_{IT} are reached, indicating a strict correlation between the oxide layer thickness and the displacement of maximum H_{IT} . The peak amplitudes are all above the bulk value $H_{IT,bulk}$ and even exceed 10 GPa in case of THERMOX-2. The latter is not surprising as the hardness of TiO_2 is known to be greater than that of metallic titanium [30]. Moreover, underneath a pronounced superficial oxide layer, a thermal diffusion zone may form, where oxygen diffuses into the lattice of the titanium metal (up to some tens of micrometers in depth). This oxygen diffusion (OD) zone may exhibit hardness values increased by up to 4–5 GPa [31].

All samples except for the fs-laser oxidized one (LASOX) exhibit an indentation hardness larger than $H_{IT,bulk}$. In contrast, for the latter sample the indentation hardness stays below the bulk value for displacements > 60 nm (see brown curve in Fig. 4a), indicating a softening of the material in the laser-processed area. However, influences of the surface topography due to the formation of LIPSS with height modulations of a few hundreds of nanometers and periods of ~ 500 – 600 nm cannot be excluded during the IIT.

Table 1 compiles the properties of the superficial oxide layers of all six samples investigated, including their thickness (VASE), material structure (μ -RS), and indentation hardness (IIT) that was averaged over the depth range between 100 and 200 nm. That range was chosen here as it is the most relevant part of the wear track (compare Sect. 3.4).

3.4 Tribological performance

To gain additional insights into the relevance of superficial oxidation, RSTT was performed at the four different thermally (Fig. 5b) and anodically oxidized (Fig. 5c) samples and compared to the polished and fs-laser irradiated titanium samples (Fig. 5a). The measurements of the COF during 1000 sliding cycles are provided in the left part of Fig. 5, while in the right part optical micrographs of the corresponding wear tracks after 1000 cycles are shown.

Figure 5a summarizes the findings previously published in Ref. [3]. The POLISHED surface results in COF's varying between 0.32 and 0.61 (dark cyan curve), while the COF in the fs-laser irradiated region (LASOX, brown curve) is significantly reduced to values between 0.12 and 0.13. These RSTT results are supported by the optical micrographs of

the wear tracks, which indicate a severe surface damage on the polished sample, while the fs-laser irradiated surface remained intact (confirmed by SEM [3], data not shown here). The COF of the POLISHED titanium sample averaged over 1000 cycles (0.47) is larger than the one of Qu et al., reporting a value of 0.37 when sliding polished Ti6Al4V alloy against gray cast iron in engine oil (regime of mixed friction, somewhat different test conditions) [31].

Figure 5b provides the RSTT results for the two thermally treated samples. For THERMOX-1 the COF is almost constant around 0.12 after about 20 cycles of running-in, similar to the result of LASOX. The wear track is hardly visible in OM. Within the experimental uncertainty, the averaged COF of THERMOX-1 (0.12) is the same as that of Qu et al., reporting a value of 0.11 in their tribological tests [31]. In contrast, for THERMOX-2 the COF gradually increases from 0.12 at the beginning to up to ~ 0.17 after 120 sliding cycles. At more than 120 cycles, the COF steeply increases to values exceeding 0.66 and continues to vary between ~ 0.3 and 0.63. The increase of the COF after ~ 120 cycles indicates a damage of the superficial oxide layer. The corresponding optical micrograph reveals a damaged surface with a wide wear track supporting that scenario.

Figure 5c shows the RSTT results for the two anodically oxidized surfaces. For both samples, strongly varying COFs can be seen (ANOX-9V: 0.30–0.58; ANOX-18V: 0.16–0.56). OM images again indicate severe surface damage associated with large wear tracks.

Table 2 summarizes the results of the RSTT performed in engine oil for all six samples. The second column indicates the upper and lower limits of the COF as measured during the 1000 sliding cycles. The third column qualifies the wear behavior of the different surfaces in comparison with the non-irradiated polished reference surface. Comparing the tribological results with the oxide layer thickness (Sect. 3.2), its crystalline structure (Sect. 3.1), and the indentation hardness (Sect. 3.3) suggests that for a beneficial tribological effect a minimal oxide layer thickness of a few hundred nanometers is required here, while the material structure (polymorph of TiO_2) or the hardness of the oxide layer are less decisive.

For visualizing the modification of material underneath a wear track of the fs-laser oxidized sample, a wear track on a Ti6Al4V sample treated at identical fs-laser-processing conditions was chosen. In previous publications, we have shown that neither the LIPSS formation nor the tribological performance are significantly different for grade-1 titanium (Ti) or grade-5 titanium alloy (Ti6Al4V) [3, 4]. Hence, the following results for the titanium alloy are also representative for pure titanium samples. Figure 6 compiles a top-view optical micrograph (a), a top-view FIB image (b), and a bright field cross-sectional STEM image (c) of the selected wear track. The green hatched area in (b) indicates size and

Fig. 5 Left: Coefficient of friction as a function of the number of cycles as obtained during RSTT of the differently oxidized grade-1 titanium samples against a 100Cr6 steel ball in engine oil. Right: Optical micrographs of the corresponding wear tracks after 1000 sliding cycles. **a** LSFL-covered surface regions after processing by fs-laser pulses in air (LASOX: brown curve). A reference spectrum of the non-irradiated sample surface is shown for comparison (POLISHED: dark cyan curve); **b** Thermally heated samples (THERMOX-1: green curve, THERMOX-2: dark yellow curve); **c** Anodically oxidized samples (ANOX-18V: black curve, ANOX-9V: purple curve). The data in **a** are taken from Ref. [3]. The scale in **a** applies for all micrographs

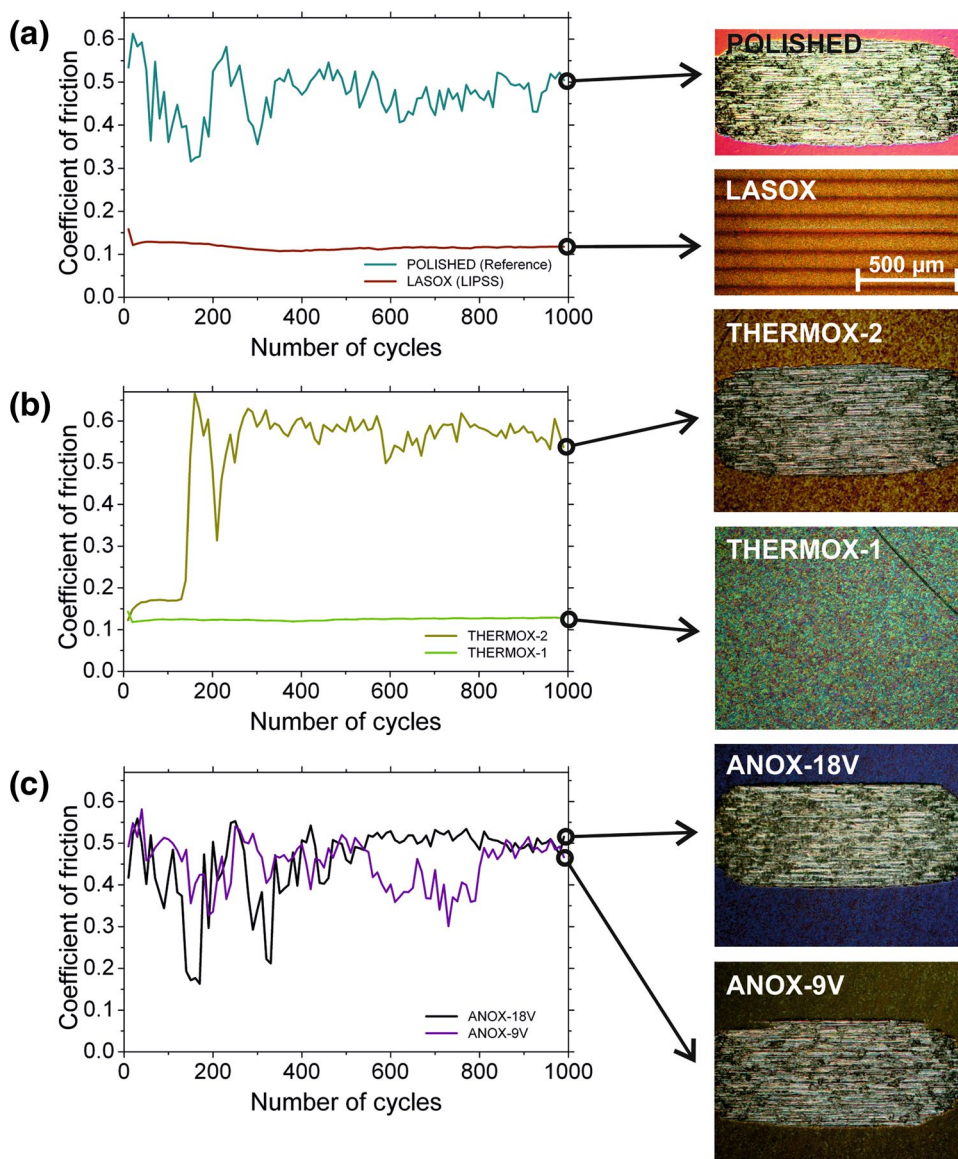


Table 2 Tribological performance of differently oxidized grade-1 titanium samples; Symbols ++, +, 0, – indicate the performance relative to the polished reference

Sample name	Coefficient of friction (COF)	Wear (after 1000 cycles)
POLISHED	0.32–0.61 [3]	Reference
LASOX	0.12–0.13 [3]	++
THERMOX-1	0.12–0.14	++
THERMOX-2	0.12–0.67	0/–
ANOX-18V	0.16–0.56	0/+
ANOX-9V	0.30–0.58	0

The range of uncertainty in the COF measurements is ± 0.02

location of the lamella cut out during the FIB sample preparation, while the upper right inset displays the FIB image of the TEM lamella. The vertical lines in Fig. 6a represent the individual laser-processing lines separated by 100 μm. In the central part of the optical micrograph, the wear track is visible as reddish colored area accompanied by a few vertical fine lines representing scratches. Both features can be identified in the magnified FIB micrograph (Fig. 6b). The lower left inset in Fig. 6b shows a $5 \times 3.6 \mu\text{m}^2$ area located in the laser processed zone outside the wear track. It resolves the almost horizontally aligned LSFL nanostructures.

The STEM image in Fig. 6c displays the cross-section of a part of the wear track in the laser-processed area (indicated by the horizontal double-arrows) and the adjacent region at the right of it (the border of the wear track is marked by the red vertical arrows). In the lower part of the image, the

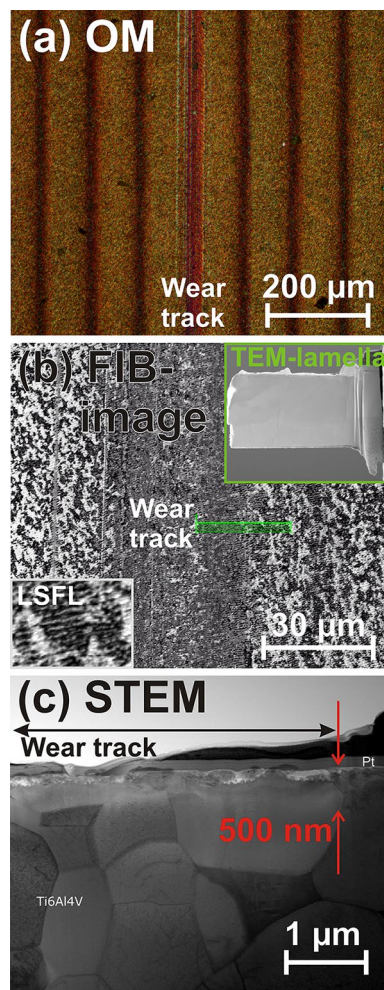


Fig. 6 Characterization of a RSTT wear track on grade-5 titanium alloy after fs-laser treatment (identical laser-processing and RSTT conditions as for the LASOX sample shown in Fig. 5); **a** optical micrograph. The dark vertical lines arise from the line wise laser beam scanning; **b** FIB image of the sample surface, the location of the lamella preparation is marked in green. The upper right inset shows the FIB image of the TEM lamella. The lower left inset shows a $5 \times 3.6 \mu\text{m}^2$ area located in the laser-processed zone outside of the wear track; **c** bright field STEM image of the cross-section of the wear track. The black double-arrow marks the extent of the wear track. The two vertical red arrows indicate the affected surface layer with a thickness of 500 nm

grain structure of the Ti6Al4V alloy is visible. The surface protecting Pt layer consisting of two sublayers is marked. It can be seen from the TEM image that a depth of less than 500 nm (as indicated by the distance between the two red vertical arrows in Fig. 6c) is affected by the laser processing and the subsequent tribological tests. Here, a significant change of contrast and a loss of the grainy Ti6Al4V microstructure are visible. The same behavior is expected for LASOX. Presumably, the thickness of the oxide layer of LASOX is larger than 200 nm (as indicated by Auger

Electron Spectroscopy in Ref. [27]) but smaller than 500 nm (as indicated by STEM in Fig. 6).

The beneficial tribological effect of thermal treatment of titanium alloy surfaces in engine oil lubricated sliding friction experiments against iron/steel is already known from the literature [31, 32]. Thermal oxidation produces an oxide layer at the surface and a hardened OD zone in the subsurface region [33]. For the reduction of friction and wear, contributions of a surface near layer including oxygen and the action of additive molecules, such as zinc-dialkyl-dithiophosphate (ZDDP, $\text{Zn}[\text{S}_2\text{P}(\text{OR})_2]_2$, with R representing a hydrocarbon alkyl chain) contained in the engine oil, have been identified (see [31] and references therein). The effects are summarized as follows: The worn oxygen diffused Ti6Al4V surface exhibits a two-layer surface boundary film, consisting of an anti-wear top film (including the elements C, O, Zn, Mg, Al, P, S, Ca, Ti, and Fe) and an oxide-rich amorphous interlayer (containing C, O, Ti, Al, V). Both layers have a thickness between 50 and 100 nm. The films are tightly bound and there is no clear interface between the interlayer and the OD zone at the titanium surface underneath ($\sim 35 \mu\text{m}$ thick for the thermally treated samples studied in reference [31]). For the formation of the anti-wear top-layer ZDDP is involved. Qu et al. suggested that a high contact pressure and the frictional heating are necessary for the ZDDP to react with the oxygen diffused titanium surface. Moreover, it was hypothesized that the OD zone is critical in the boundary film formation as it supplies a surplus of oxygen to in-situ form a renewable oxide interlayer with a higher reactivity than the metal to react with the additives in the lubricant. The anti-wear film cannot form on a polished surface even though it has a native oxide layer. This natural oxide layer is too thin and lacks a strong support from the softer metal. Therefore, it cannot survive the wear process [31]. Similar effects were reported for the tribological activity of ZDDP on ferrous materials, which were historically driving the technological development and optimization of ZDDP containing engine oils [34].

In view of the RSTT experiments performed in this work, the following aspects should be mentioned:

- (i) In our different oxidation experiments, a beneficial tribological effect was reported solely for oxide layer thicknesses larger than ~ 150 nm. It is likely that this oxide layer plays the same role as the OD layer, i.e., supplying oxygen in the tribo-contact area for forming the amorphous interlayer and the anti-wear-film.
- (ii) As shown in Ref. [27], the laser processing is accompanied by the formation of graded oxide layers without sharp interfaces. For the LASOX sample, this may help to mechanically stabilize the oxygen containing near surface region, preventing its spallation/delamination during the RSTT.

- (iii) The topographical modulation depth of the LIPSS nanostructures (LSFL) of a few hundreds of nanometers is of similar size as the ball-sample deformation during the RSTT. This may help to confine the lubricant in the tribological contact area of the LASOX sample during RSTT.

4 Conclusions

Commercial grade-1 titanium samples were polished and oxidized by three different methods (fs-laser processing, thermal treatment, anodic oxidation). The oxidized surfaces were characterized by scanning electron microscopy, micro Raman spectroscopy, variable angle spectroscopic ellipsometry, instrumented indentation testing, reciprocating sliding tribological tests, and scanning transmission electron microscopy. Depending on the treatment and processing conditions, the oxidation leads to the formation of superficial TiO₂-layers with different material structure, hardness, and thickness varying between a few nanometers (polished reference) and a few hundreds of nanometers. In RSTT, only the titanium samples with oxide layer thicknesses exceeding ~ 150 nm featured an improved tribological performance, i.e., lower COFs and reduced wear. This confirms that a minimum oxygen-containing layer thickness is required together with the additive ZDDP of the engine oil to form a sufficiently thick anti-wear layer during RSTT, which prevents a direct metal–metal contact of the two sliding tribological bodies.

Acknowledgements The Authors would like to thank S. Binkowski (BAM 6.3) for polishing the titanium samples, N. Zadeh (BAM 5.5) for the thermal sample processing, and S. Benemann (BAM 6.1) for the SEM characterizations. This work has received funding from the German Science Foundation (DFG) under grant no. KR 3638/1–2 and from the Horizon 2020 European Union’s research and innovation programme under grant agreement No. 665337 (“LiNaBioFluid”; URL: <http://www.laserbiofluid.eu>).

Open Access This article is distributed under the terms of the Creative Commons Attribution 4.0 International License (<http://creativecommons.org/licenses/by/4.0/>), which permits unrestricted use, distribution, and reproduction in any medium, provided you give appropriate credit to the original author(s) and the source, provide a link to the Creative Commons license, and indicate if changes were made.

References

1. A.F. Hollemann, E. Wiberg, N. Wiberg eds. *Inorganic chemistry*. (Academic Press, San Diego, 2001)
2. J. Bonse, R. Koter, M. Hartelt, D. Spaltmann, S. Pentzien, S. Höhm, A. Rosenfeld, J. Krüger, *Appl. Phys. A* **117**, 103 (2014)
3. J. Bonse, R. Koter, M. Hartelt, D. Spaltmann, S. Pentzien, S. Höhm, A. Rosenfeld, J. Krüger, *Appl. Surf. Sci.* **336**, 21 (2015)
4. J. Bonse, S. Höhm, M. Hartelt, D. Spaltmann, S. Pentzien, R. Koter, S. Marschner, A. Rosenfeld, J. Krüger, in *Femtosecond laser-induced surface nanostructures for tribological applications*, *Optically induced nanostructures: biomedical and technical applications*, ed by A. Ostendorf, K. König (Walter de Gruyter, 2015), (Chap. 7)
5. J. Bonse, J. Krüger, S. Höhm, A. Rosenfeld, *J. Laser Appl.* **24**, 042006 (2012)
6. J. Bonse, S. Höhm, S.V. Kirner, A. Rosenfeld, J. Krüger, *IEEE J. Sel. Top. Quantum Electron.* **23**, 9000615 (2017)
7. A. Rudenko, J.-P. Colombier, S. Höhm, A. Rosenfeld, J. Krüger, J. Bonse, T.E. Itina, *Sci. Rep.* **7**, 12306 (2017)
8. B. Johs, J.A. Woollam, C.M. Herzinger, J.N. Hilfiker, R.A. Synowicki, C.L. Bungay, *Proc. SPIE* **10294**, 1029404 (1999)
9. W.C. Oliver, G.M. Pharr, *J. Mater. Res.* **19**, 3 (2004)
10. ISO 14577 Metallic materials—*instrumented indentation test for hardness and materials parameters—Part 1: test method (2015) and Part 4: test method for metallic and non-metallic coatings (2016)*
11. B.N. Lucas, W.C. Oliver, J.E. Swindeman, in *Fundamentals of nanoindentation and nanotribology book series: materials research society symposium proceedings* **522**, 3, (1998)
12. X. Li, B. Bhushan, *Mater. Charact.* **48**, 11 (2002)
13. J. Hay, P. Agee, E. Herbert, *Exp. Tech.* **43**, 86 (2010)
14. S. Fouvry, C. Paulin, *Wear* **319**, 211 (2014)
15. J. Bonse, S. Höhm, R. Koter, M. Hartelt, D. Spaltmann, S. Pentzien, A. Rosenfeld, J. Krüger, *Appl. Surf. Sci.* **374**, 190 (2016)
16. R.M. Langford, M. Roger, *Micron* **39**, 1325 (2008)
17. D. Velten, V. Biehl, F. Aubertin, B. Valeske, W. Possart, J. Breme, *J. Biomed. Mater. Res.* **59**, 18 (2002)
18. E. Gemelli, N.H.A. Camargo, *Revista Matéria (Rio J.)* **12**, 525 (2007)
19. R.J. Nemanich, C.C. Tsai, G.A.N. Conell, *Phys. Rev. Lett.* **44**, 273 (1980)
20. E.C. Landis, K.C. Phillips, E. Mazur, C.M. Friend, *J. Appl. Phys.* **112**, 063108 (2012)
21. T. Shinonaga, M. Tsukamoto, T. Kawa, P. Chen, A. Nagai, T. Hanawa, *Appl. Phys. B* **119**, 493 (2015)
22. Y.-H. Zhang, C.K. Chan, J.F. Porter, W. Gao, *J. Mater. Res.* **13**, 2602 (1998)
23. O. Madelung, U. Rössler, M. Schultz (eds) *Titanium oxide (TiO₂): properties of vibrational and Raman modes in rutile*, in *Landolt-Börnstein, New series group III condensed matter, numerical data and functional relationships in science and technology*, vol. 41D (Springer, 2000)
24. O. Madelung, U. Rössler, M. Schultz (eds) *Titanium oxide (TiO₂): physical properties of anatase*, in *Landolt-Börnstein, new series group III condensed matter, numerical data and functional relationships in science and technology*, vol. 41D (Springer, 2000)
25. B. von Blanckenhagen, D. Tonova, J. Ullmann, *Appl. Opt.* **41**, 3137 (2002)
26. A.S. Ferlauto, G.M. Ferreira, J.M. Pearce, C.R. Wronski, R.W. Collins, X. Deng, G. Ganguly, *J. Appl. Phys.* **92**, 2424 (2002)
27. S.V. Kirner, T. Wirth, H. Sturm, J. Krüger, J. Bonse, *J. Appl. Phys.* **122**, 104901 (2017)
28. J. Bonse, J. Krüger, *J. Appl. Phys.* **107**, 054902 (2010)
29. F.K. Mante, G.R. Baran, B. Lucas, *Biomaterials* **20**, 1051 (1999)
30. A. Bendavid, P.J. Martin, H. Takikawa, *Thin Solid Films* **360**, 241 (2000)
31. J. Qu, P.J. Blau, J.Y. Howe, H.M. Meyer, *Scr. Mater.* **60**, 886 (2009)
32. D.G. Bansal, O.L. Eryilmaz, P.J. Blau, *Wear* **271**, 2006 (2011)
33. R. Bailey, Y. Sun, *Wear* **308**, 61 (2013)
34. M.A. Nicholls, T. Do, P.R. Norton, M. Kasrai, G.M. Bancroft, *Tribol. Int.* **38**, 15 (2005)